REDUCED-ORDER MODELLING OF EFFECTIVE CONTACT AREA IN SOFC STACK ASSEMBLY

Klein Florian

Section – MECHANICAL ENGINEERING
Faculty of mechanical engineering, Year 2
Master's study programme – APPLIED MECHANICS

Abstract: Solid oxide fuel cell (SOFC) stacks require uniform interfacial contact to maintain low electrical resistance and mechanical integrity. This paper presents a multi-level framework for predicting effective contact area in SOFC stack assembly, combining two experimental campaigns, a geometric reduced-order model (ROM), and a force-equilibrium pressure-map extension. The geometric ROM predicts contact maps, contact area, and contact fraction from surface topography inputs via a closure-based thresholding approach. A Latin Hypercube Sampling (LHS) sensitivity study with 500 samples identifies surface waviness and roughness amplitudes as the dominant drivers of progressive contact growth, with global wafer warpage playing a secondary role. The force-equilibrium extension normalises the predicted pressure field to satisfy global force balance, providing apparent contact-pressure maps at a prescribed assembly load. A staged multi-SRU extension with sample-level viability conditioning, evaluated over 500 Monte Carlo samples of a ten-SRU stack, quantifies the operational robustness of the assembly process and identifies persistent SRU-specific weak zones under realistic tolerance variability.

Keywords: SOFC, contact mechanics, reduced-order model, surface topography, sensitivity analysis, stack assembly, force-equilibrium

1 Introduction

Solid oxide fuel cells (SOFCs) are high-temperature electrochemical converters operating at 650 °C to 900 °C. Their high electrical efficiency, fuel flexibility, and suitability for combined heat and power make them a compelling technology in the transition toward decarbonised energy systems [1, 2]. Long-term durability, however, remains the primary commercialisation barrier.

In a planar SOFC stack, each stack repeating unit (SRU) consists of a thin ceramic wafer (a multilayer laminate of anode support, electrolyte, and cathode) clamped between a ribbed metallic interconnect and a backplate (Fig. 1). The quality of mechanical contact at the wafer–interconnect interface is critical on multiple levels. Electrically, non-uniform contact elevates the interfacial contact resistance (ICR), which reduces stack efficiency and generates local Joule heating. Mechanically, non-uniform contact pressure creates stress concentrations in the brittle ceramic wafer, increasing the risk of fracture and delamination. Thermally, inadequate contact reduces effective heat conduction across the interface, amplifying thermal gradients and accelerating thermo-mechanical fatigue [3].

The effective contact area at assembly is governed by the interplay of several geometric factors: wafer warpage arising from the laminate sintering process, surface waviness and roughness at multiple length scales, geometric tolerances of the backplate and interconnect, and the applied assembly force. Disentangling the relative contribution of each factor is non-trivial:

high-fidelity three-dimensional finite element (FE) contact simulations can resolve these effects in detail but are computationally expensive, making them impractical for the broad parameter and variability studies required in an industrial design context.

This paper addresses this gap by presenting a reduced-order modelling framework that is computationally efficient, parametrically flexible, and anchored to experimentally defined observables. The framework proceeds from two experimental campaigns that define the relevant observables, to a geometric contact ROM for rapid variability analysis, to a force-equilibrium pressure-map extension.

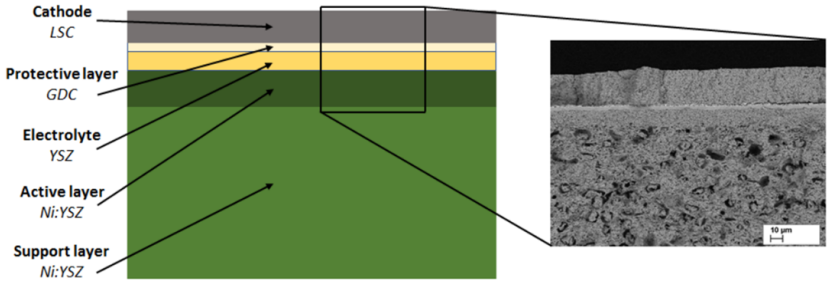

Figure 1: Cross-section of a planar SOFC showing the layered cell architecture and the contact interfaces between wafer, interconnect, and backplate.

2 Experimental Reference

Two complementary experiments were conducted on single SRU specimens to define experimentally measurable observables against which the ROM predictions can be evaluated.

Force-to-full-contact campaign. A universal testing machine (UTM) was used to apply progressive compressive loading to the SRU while recording force and crosshead displacement. The test was repeated across multiple specimens with varying warpage levels and warpage orientations. Figure 2 shows the measured force–displacement curves for all tested specimens. The curves exhibit a characteristic shape: a low-stiffness initial regime corresponding to progressive closure of the initial gap, followed by a sharp stiffness increase once macro-contact is established across the wafer. The force-to-full-contact is consistent across specimens regardless of warpage direction, confirming that the contact closure is not sensitive to the sign or orientation of the global warp.

Contact footprint campaign. A pressure-sensitive transfer tape was placed at the wafer–backplate interface and the assembly was loaded in a controlled manner. The tape produces a visible imprint in regions where contact pressure exceeds its activation threshold, providing direct spatial information about the contact footprint. A custom backplate was 3D-printed from PETG to serve as a repeatable and geometrically representative contact counterpart (Fig. 3a). The resulting imprints (Fig. 3b) confirm that contact initiates at localised patches consistent with the local surface topography and progressively expands with increasing load, consistent with the progressive closure mechanism captured by the ROM.

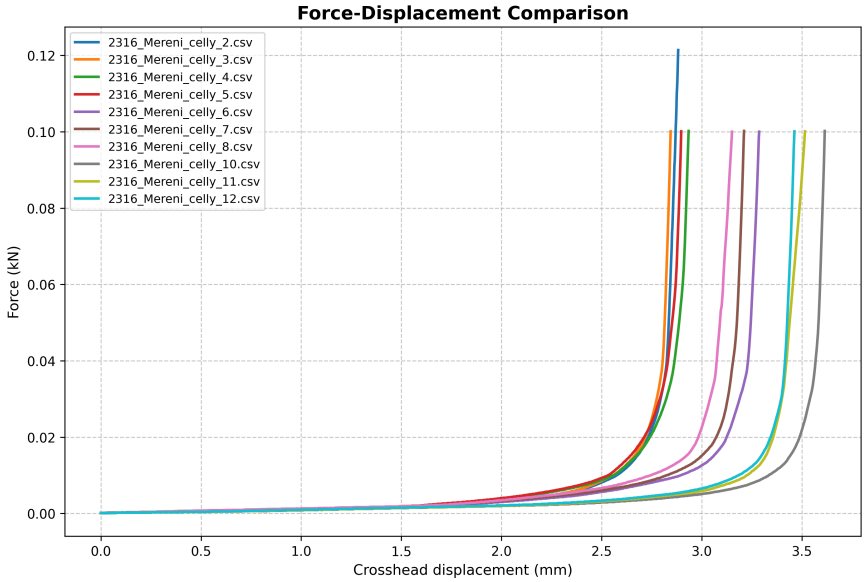

Figure 2: Force–displacement curves from the UTM campaign across multiple SRU specimens. All curves exhibit the same characteristic transition from progressive closure to stiff full-contact response, with the transition point largely insensitive to warpage orientation.

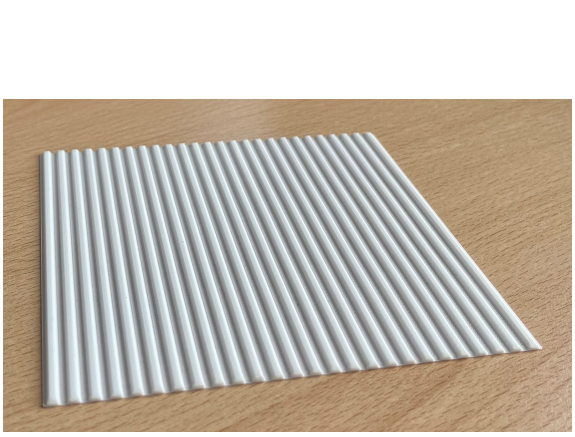

(a) 3D-printed PETG ribbed backplate

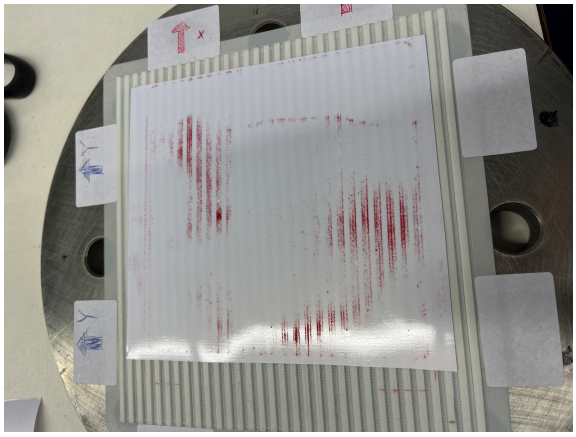

(b) Pressure-tape contact imprint

Figure 3: Contact footprint experiment: (a) additive-manufactured PETG backplate; (b) pressure-transfer tape imprint at a representative compressive load showing localised and spatially distributed contact patches.

3 Geometric Reduced-Order Model

3.1 Model formulation

The geometric ROM predicts the contact state at a given interface closure c from the surface height map $z(x, y)$ and the counterface geometry. Contact is treated as a geometric thresholding problem: a pixel (i, j) of the discretised interface is considered in contact if and only if the relative height $z_{\text{rel}}(x, y)$ meets or exceeds the closure:

$$\mathbf{1}_{ij}(c) = \begin{cases} 1 & \text{if } z_{\text{rel},ij} \geq c \\ 0 & \text{otherwise} \end{cases} \tag{1}$$

For a flat counterface, $z_{\text{rel}}(x, y) = z(x, y)$. For a ribbed counterface with rib land width w, rib gap g, and rib depth d, a binary rib mask $m(x, y) \in \{0, 1\}$ is introduced and the counterface height field is:

$$z_{\text{cf}}(x, y) = \begin{cases} 0 & m(x, y) = 1 \quad \text{(rib land)} \\ -d & m(x, y) = 0 \quad \text{(rib gap)} \end{cases} \tag{2}$$

so that $z_{\text{rel}}(x, y) = z(x, y) - z_{\text{cf}}(x, y)$. When contact in rib gaps is excluded by assumption, the maximum achievable contact fraction is bounded by the rib coverage ratio:

$$f_{\text{max}} \leq \eta_{\text{rib}} = \frac{w}{w + g} \tag{3}$$

The contact area and contact fraction at closure c are computed as:

$$A(c) = \sum_{i,j} \mathbf{1}_{ij}(c)\, \Delta x\, \Delta y, \qquad f(c) = \frac{A(c)}{A_{\text{nom}}} \tag{4}$$

where A_{nom} is the nominal interface area and Δx, Δy are the pixel dimensions of the height map.

The model intentionally excludes elastic deformation, frictional traction, adhesion, and creep. Its outputs are therefore interpreted as geometric contact metrics suitable for trend analysis, sensitivity studies, and relative comparison, rather than as fully validated absolute force–pressure predictions.

3.2 Surface topography model

For sensitivity studies where measured height maps are not available, the wafer surface is synthesised as a superposition of three components:

$$z(x, y) = z_{\text{warp}}(x, y) + z_{\text{wav}}(x, y) + z_{\text{rough}}(x, y) \tag{5}$$

z_{warp} is a smooth global form (bowl or saddle) with amplitude a_{warp} and a fixed sign convention $z_{\text{warp}} = -a_{\text{warp}}\, b(x, y)$, where $b(x, y)$ is a normalised base shape. z_{wav} and z_{rough} are correlated Gaussian random fields generated via filtered white noise, with prescribed RMS amplitudes (R_q^{wav}, R_q^{rough}) and spatial correlation lengths (λ_{wav}, λ_{rough}). This parametric decomposition allows independent variation of each topographic scale, enabling the sensitivity study described in Section 4.

3.3 Contact map outputs

Figure 4 illustrates the effect of topographic complexity on the predicted contact maps. With only global warpage, the contact state transitions abruptly from near-zero to full contact as closure increases: the surface either clears the threshold everywhere or nowhere within a narrow closure range. Adding multi-scale waviness and roughness transforms this behaviour into a progressive, spatially distributed contact growth, in which individual patches engage sequentially as closure increases. This is consistent with the experimental footprint observations and with classical rough-surface contact theory, which predicts approximately linear growth of real contact area with load in the multi-asperity regime [4].

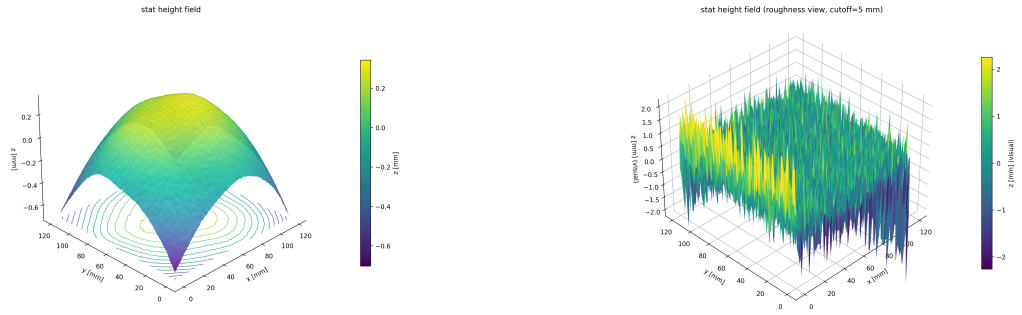

(a) Smooth surface (warpage only)

(b) Surface with waviness and roughness

Figure 4: ROM contact maps for a flat counterface at a representative closure. Adding multi-scale topography converts the abrupt warpage-driven transition into progressive, spatially distributed contact growth.

4 Topographic Drivers of Contact Formation

4.1 Latin Hypercube Sampling sensitivity study

To quantify the relative importance of each topographic parameter, a Latin Hypercube Sampling (LHS) study was conducted over a six-dimensional input space: warpage amplitude a_{warp}, waviness RMS R_q^{wav}, waviness correlation length λ_{wav}, roughness RMS R_q^{rough}, roughness correlation length λ_{rough}, and interface tilt. A design of $N = 500$ space-filling samples was generated, the ROM was evaluated at a representative closure for each sample, and Spearman rank correlation coefficients between each input and the mean contact fraction were computed as the sensitivity metric. Spearman rank correlation is non-parametric and monotone-relationship sensitive, making it robust to the nonlinear input–output mapping of the ROM.

Figure 5 shows the resulting sensitivity ranking. Surface waviness and roughness amplitudes are the primary determinants of contact fraction, while global wafer warpage amplitude ranks last among the six inputs examined. This finding is consistent with classical rough-surface contact theory: in the multi-asperity regime, contact area is governed by the local height distribution rather than the global form of the wafer [4]. The implication for tolerance design is that surface finish specifications are at least as critical as wafer flatness requirements.

4.2 Closure-dependent sensitivity

The sensitivity ranking evolves with the interface closure. Figure 6 shows the absolute effect size of the three most influential parameters as a function of closure. At low closure values (near contact onset), the effects are broadly comparable. As closure increases, the contribution of counterface roughness R_q^{plate} grows rapidly and dominates at larger closures, while the wafer roughness effect remains comparatively flat. This behaviour reflects the geometry of progressive asperity engagement: at larger closures, the counterface surface structure increasingly controls which additional regions enter contact.

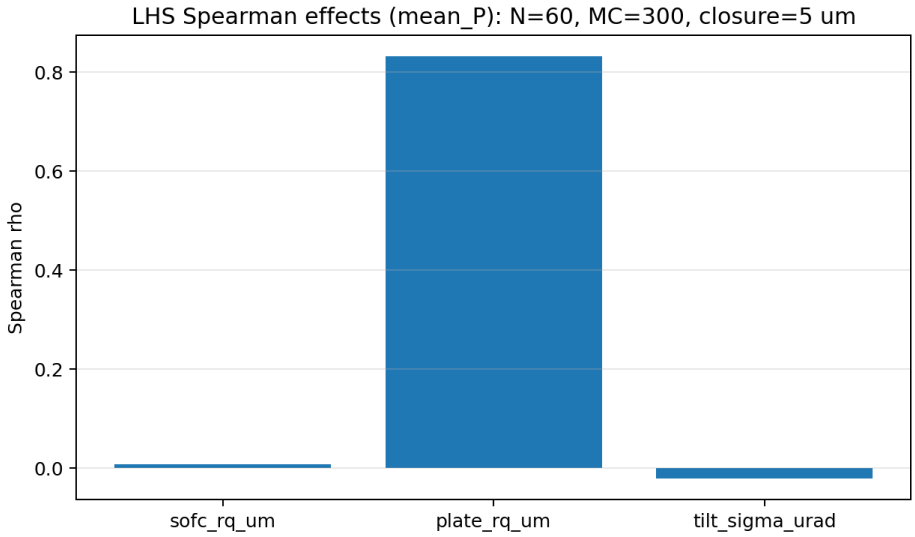

Figure 5: Spearman rank correlation between each topographic input and mean contact fraction (500 LHS samples at a representative closure). Waviness and roughness RMS amplitudes dominate; global warpage amplitude ranks lowest.

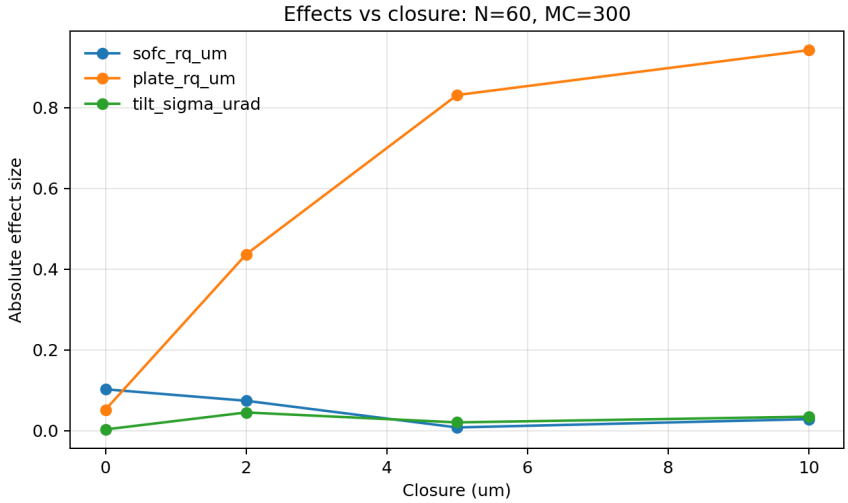

Figure 6: Absolute effect size of the dominant topographic parameters as a function of interface closure. Counterface roughness grows strongly with closure and dominates at higher closure values.

4.3 Conditional contact probability maps

To visualise the spatial manifestation of parameter sensitivity, conditional contact probability maps were generated by binning the 500 LHS samples by counterface form error amplitude and averaging the contact maps within each bin (Fig. 7). The spatial rib pattern is preserved by construction, but the contact probability level on the admissible rib lands increases consistently with the bin index, confirming the scalar sensitivity ranking in a spatially resolved representation. This type of output provides design-relevant spatial information: it identifies which interface regions are most sensitive to manufacturing variability and where contact robustness is lowest.

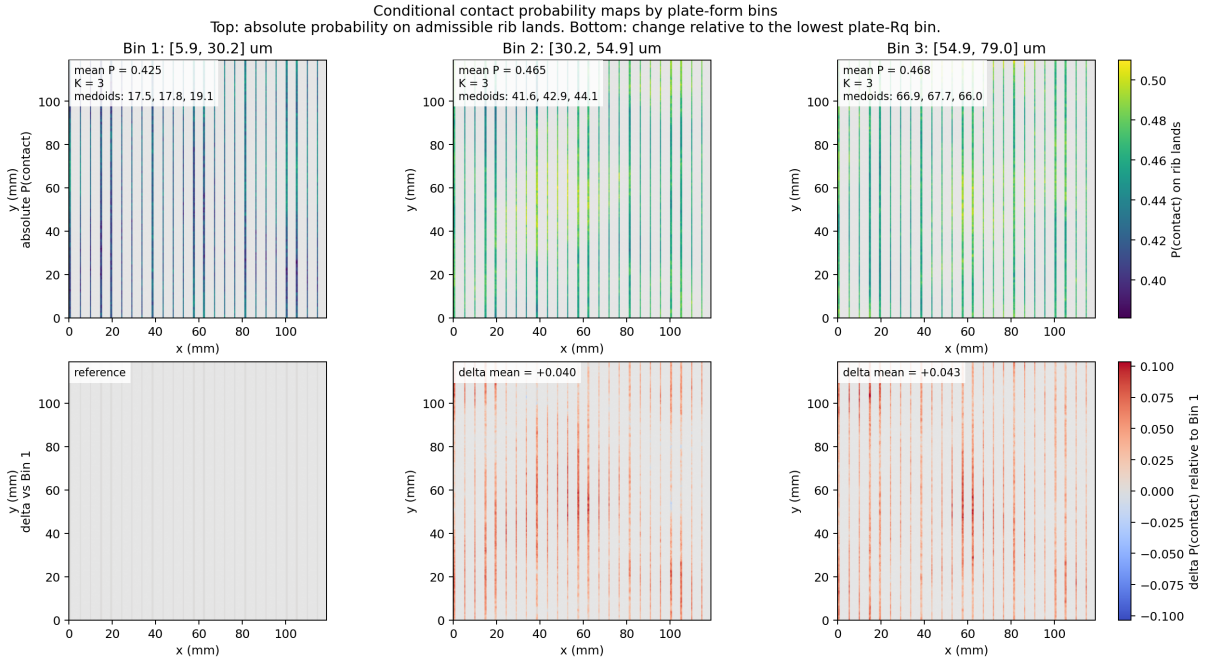

Figure 7: Conditional contact probability maps binned by counterface form error amplitude (three bins, low to high). Top row: absolute contact probability on rib lands. Bottom row: change relative to the lowest bin. Contact probability on rib lands increases with form error, consistent with the sensitivity ranking.

5 Stack-Level Analysis

The SRU-level ROM predicts contact at a single interface, but a real SOFC stack is assembled in two distinct stages – each SRU is first pre-compressed individually and then the assembled stack is compressed as a unit – and the resulting contact distribution is influenced by tolerance accumulation, assembly misalignment, and SRU-to-SRU thickness scatter that do not appear at the single-SRU level. To address this, the geometric ROM is lifted to a staged multi-SRU formulation with sample-level viability conditioning.

5.1 Multi-SRU closure formulation

For a realized stack geometry and Monte Carlo sample k, the final-stage closure field of SRU i is decomposed as

$$z_i^{(k)}(x,y) = h_{\text{sofc},i}(x,y) - g_{\text{plate},i}(x,y) - g_{\text{asm}}^{(k)}(x,y) + w_{\text{stack}}(x,y) + w_i(x,y) + \Delta t_i^{(k)} + s_i, \quad (6)$$

where $h_{\text{sofc},i}$ is the SRU-local short-wavelength topography, $g_{\text{plate},i}$ the mating-plate form deviation, $g_{\text{asm}}^{(k)}$ sample-dependent assembly offset and tilt, w_{stack} a shared stack-level low-frequency field, w_i an SRU-local low-frequency field, $\Delta t_i^{(k)}$ a scalar thickness-related closure shift, and s_i a residual seating shift inherited from the SRU pre-compression stage. Contact is predicted by the same thresholding logic as in Section 3, with admissibility restricted to rib lands. Uncertainty is resolved at two levels: a fixed realized stack geometry represents one plausible manufactured stack, and a Monte Carlo ensemble over assembly/load variability represents the production population.

5.2 Viability conditioning

To exclude clearly non-functional assemblies from the reported statistics, a sample-level viability filter is applied: a sample is accepted only if the stack-mean and per-SRU contact fractions both exceed prescribed minima. The viable-conditioned contact probability for SRU i is

$$P_{c,i}^{\text{viable}}(x,y) = \frac{1}{N_{\text{acc}}} \sum_{k \in \mathcal{A}} \chi_i^{(k)}(x,y), \tag{7}$$

where $\mathcal{A}$ is the set of accepted samples, $N_{\text{acc}} = |\mathcal{A}|$, and $\chi_i^{(k)}$ is the binary contact map for sample k. This conditioning does not alter the underlying contact logic; it changes the population over which the reported probability is interpreted to that of operationally viable stacks.

5.3 Production results

The production ensemble comprised a ten-SRU stack, five realized-stack seeds, and 100 Monte Carlo samples per seed (500 samples total). The interface was discretized on a 256×256 grid over a 119 mm wafer with a ribbed counterface of 0.65 mm rib width and 4.12 mm gap; the final closure threshold was 6 µm and the viability thresholds were 0.22 (stack mean) and 0.18 (per SRU). The ensemble-mean accepted-sample fraction after viability filtering was 0.538, with a range of 0.49 to 0.61 across the five realized stacks, indicating that roughly half of all sampled assemblies are operationally viable under the assumed tolerance population.

Figure 8 shows viable-conditioned contact-probability maps for one representative realized stack from the production ensemble. Contact remains confined to the rib-support pattern by construction; within that pattern, the probability level varies spatially, and individual SRUs exhibit clearly distinct weak zones (dark patches and asymmetric distributions visible in SRUs 2, 5, and 10). This persistence of SRU-specific weak zones is the practical output: it identifies which interface regions in which SRUs are systematically more prone to insufficient contact under realistic assembly variability, and provides a directly actionable risk map for assembly-process design.

6 Force-Equilibrium Pressure-Map Extension

The geometric ROM described in Section 3 predicts contact maps from prescribed closure, but does not associate a physical force with a given contact state. To bridge this gap, a force-equilibrium extension was formulated in which the assembly force is prescribed instead of the closure, and the contact pressure field is determined by normalising the overlap field to satisfy global force balance.

For a prescribed normal force F and a contact map $\mathbf{1}_{ij}$ generated at the corresponding closure, the apparent contact pressure at each in-contact pixel is:

$$p_{ij} = \frac{F \cdot \delta_{ij}}{\sum_{i,j} \delta_{ij} \, \Delta x \, \Delta y} \tag{8}$$

where $\delta_{ij} = \max(z_{\text{rel},ij} - c,\, 0)$ is the local overlap at closure c, used as a proxy for local compliance. The pressure field is explicitly normalised so that $\sum_{i,j} p_{ij} \, \Delta x \, \Delta y = F$.

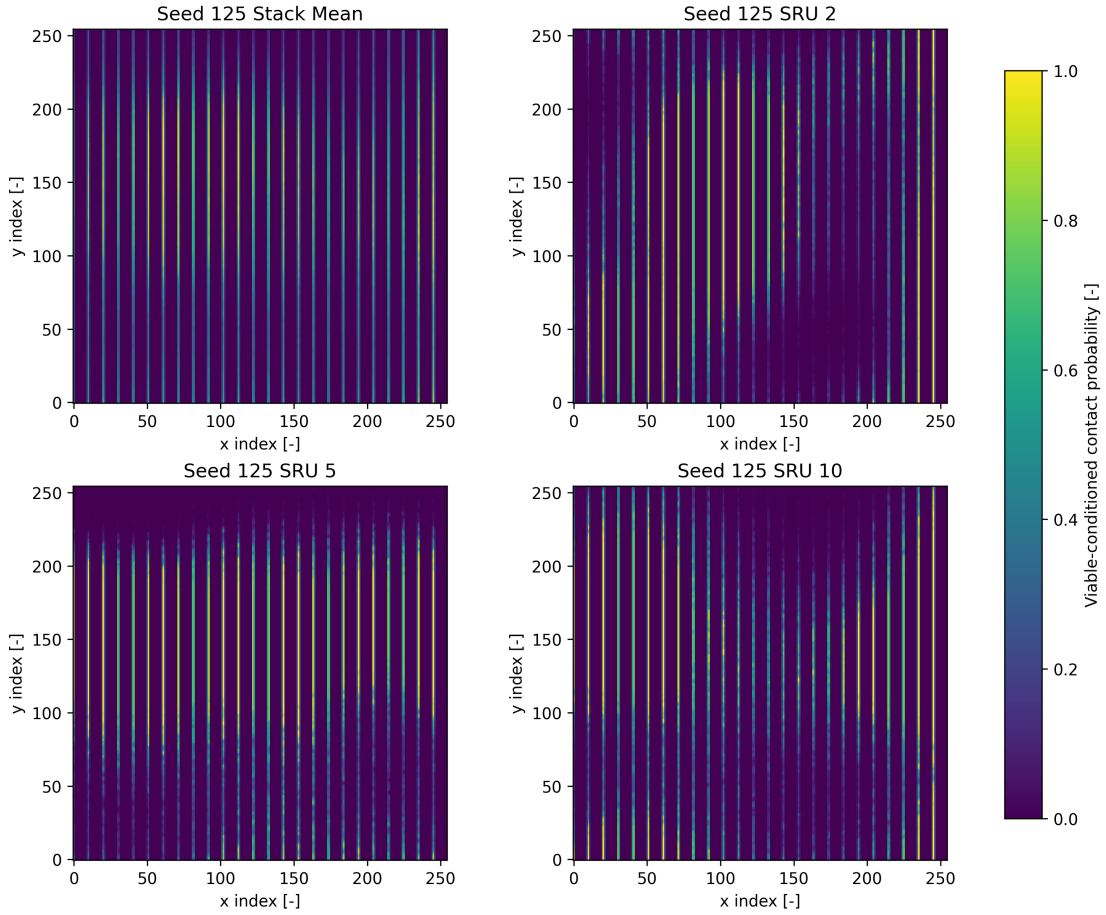

Figure 8: Viable-conditioned contact probability maps for a representative realized stack from the production ensemble (seed 125, 100 Monte Carlo samples). Stack-mean map and three SRU-level maps are shown; SRU-specific weak zones and asymmetric contact patterns are visible on the rib lands, identifying systematic risk regions under realistic assembly variability.

Figure 9 shows the resulting dashboard output for a representative ribbed-counterface case at $F = 1000\,\mathrm{N}$, serving as an apparent contact-pressure descriptor that captures pressure non-uniformity without a full elastic contact solution.

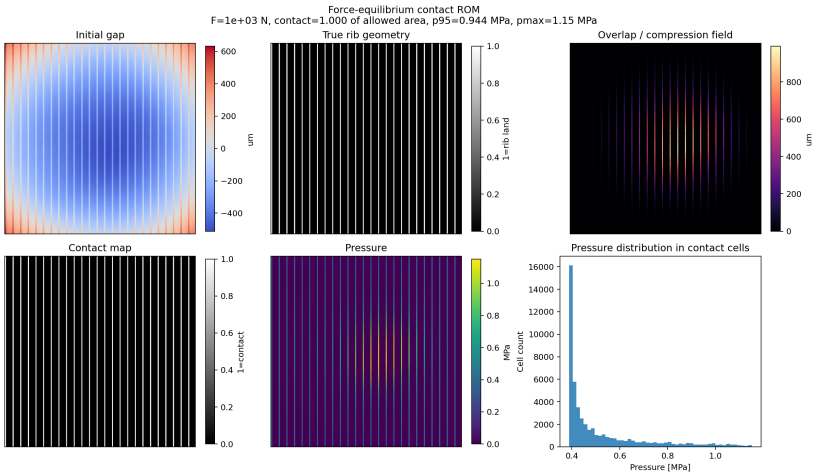

Figure 9: Force-equilibrium ROM output for a ribbed counterface at $F = 1000\,\mathrm{N}$: initial gap, contact map on rib lands, overlap/compression field, spatial pressure distribution, and pressure histogram.

7 Conclusion

This paper presented a multi-level reduced-order modelling framework for effective contact area prediction in SOFC stack assembly. The framework combines two experimental campaigns providing force-to-full-contact and contact footprint observables, a geometric ROM for rapid contact-map and contact-fraction prediction, a parametric sensitivity study, and a force-equilibrium pressure-map extension.

The central finding is that surface topography (waviness and roughness amplitudes) dominates over global wafer warpage as a driver of effective contact area at typical assembly closures. This has a direct implication for stack design: surface finish tolerances are at least as important as flatness specifications in determining the quality of interfacial contact.

The force-equilibrium extension provides apparent pressure maps at a prescribed assembly force, bridging the geometric ROM and a full elastic contact solution. The staged multi-SRU extension with viability conditioning lifts the framework from a single interface to a full stack and quantifies operational robustness: under the assumed tolerance population, roughly half of all sampled assemblies are viable, and persistent SRU-specific weak zones remain identifiable in the contact-probability maps. The framework is computationally efficient and experimentally anchored, making it directly applicable to tolerance specification and contact-risk assessment in an industrial SOFC stack development context.

References

[1] SINGHAL, S.C. and KENDALL, K. *High Temperature Solid Oxide Fuel Cells: Fundamentals, Design and Applications*. Elsevier Science, 2003.

[2] O'HAYRE, R., CHA, S.-W., COLELLA, W. and PRINZ, F.B. *Fuel Cell Fundamentals*, 3rd ed. John Wiley & Sons, 2016.

[3] NAKAJO, A., et al. Mechanical reliability and durability of SOFC stacks. Part II. *Int. J. Hydrogen Energy*, 2012, vol. 37, pp. 9269–9286.

[4] GREENWOOD, J.A. and WILLIAMSON, J.B.P. Contact of nominally flat surfaces. *Proceedings of the Royal Society of London. Series A*, 1966, vol. 295, no. 1442, pp. 300–319.